

**This item is the archived peer-reviewed author-version of:**

Micro to nano : multiscale IR analyses reveal zinc soap heterogeneity in a 19th-century painting by Corot

**Reference:**

Ma Xiao, Pavlidis Georges, Dillon Eoghan, Beltran Victoria, Schwartz Jeffrey J., Thoury Mathieu, Borondics Ferenc, Sandt Christophe, Kjoller Kevin, Berrie Barbara H., ...- Micro to nano : multiscale IR analyses reveal zinc soap heterogeneity in a 19th-century painting by Corot  
Analytical chemistry - ISSN 1520-6882 - Washington, 94:7(2022), p. 3103-3110  
Full text (Publisher's DOI): <https://doi.org/10.1021/ACS.ANALCHEM.1C04182>  
To cite this reference: <https://hdl.handle.net/10067/1873800151162165141>

# Micro to nano: multiscale IR analyses reveal zinc soap heterogeneity in a 19th century painting by Corot

Xiao Ma<sup>[a]</sup>, Georges Pavlidis<sup>[b]+</sup>, Eoghan Dillon<sup>[c]+</sup>, Victoria Beltran<sup>[d]+-</sup>, Jeffrey J. Schwartz<sup>[b,e]</sup>, Mathieu Thoury<sup>[d]</sup>, Ferenc Borondics<sup>[f]</sup>, Christophe Sandt<sup>[f]</sup>, Kevin Kjoller<sup>[c]</sup>, Barbara H. Berrie<sup>\*[g]</sup>, and Andrea Centrone<sup>\*[b]</sup>

[a] Institute for the Conservation of Cultural Heritage, Shanghai University, No.333 Nanchen Road, Shanghai, 200444, China.

[b] Nanoscale Device Characterization Division, Physical Measurement Laboratory, National Institute of Standards and Technology, 100 Bureau Drive, Gaithersburg, MD, 20899, USA.

[c] Photothermal Spectroscopy Corporation, 325 Chapala Street, Santa Barbara, CA, 93101, USA.

[d] IPANEMA, CNRS, ministère de la Culture et de la Communication Université de Versailles Saint-Quentin-en-Yvelines, USR 3461, Université Paris-Saclay, 91128 Gif-sur-Yvette, France.

[e] Institute for Research in Electronics and Applied Physics, University of Maryland, College Park, Maryland 20742, USA

[f] Synchrotron SOLEIL, L'Orme des Merisiers Saint-Aubin BP 48 91192 Gif-sur-Yvette Cedex, France.

[g] Scientific Research Department, National Gallery of Art, 2000B South Club Drive, Landover, Maryland, 20785, USA.

[+] These authors contributed equally to the manuscript

[~] Present address: AXES, Department of Physics, University of Antwerp, Groenenborgerlaan 171, B-2020 Antwerp, Belgium.

---

**ABSTRACT:** Formation and aggregation of metal carboxylates (metal soaps) can degrade the appearance and integrity of oil paints. Endeavors to understand the root cause of metal soap formation have been hampered by the limited spatial resolution of Fourier transform infrared microscopy ( $\mu$ -FTIR). We overcome this limitation using optical photothermal infrared spectroscopy (O-PTIR) and photothermal induced resonance (PTIR), two novel methods that provide IR spectra with  $\approx 500$  nm and  $\approx 10$  nm spatial resolution, respectively. The distribution of chemical phases in thin sections from the top layer of a nineteenth-century painting are investigated at multiple scales ( $\mu$ -FTIR  $\approx 10^2 \mu\text{m}^3$ , O-PTIR  $\approx 10^{-1} \mu\text{m}^3$ , PTIR  $\approx 10^{-5} \mu\text{m}^3$ ). The paint samples analyzed here are found to be mixtures of pigments (cobalt green, lead white), cured oil, and a rich array of intermixed, small (often  $\ll 0.1 \mu\text{m}^3$ ) zinc soaps domains. We identify Zn stearate and Zn oleate crystalline soaps with characteristic narrow IR peaks ( $\approx 1530$ - $1558 \text{ cm}^{-1}$ ) and a heterogeneous, disordered, water-permeable, tetrahedral zinc soap phase, with a characteristic broad peak centered at  $\approx 1596 \text{ cm}^{-1}$ . We show that the high signal-to-noise ratio and spatial resolution afforded by O-PTIR is ideal to identify phase-separated (or locally-concentrated) species with low average concentration while PTIR provides an unprecedented nanoscale view of distributions and associations of species in paint. This newly accessible nano-compositional information will advance our knowledge of chemical processes in oil paint and will stimulate new art conservation practices.

---

Oil paint can last for centuries but is not inert. Slow chemical reactions between the paint constituents and/or with environmental agents, may lead to deterioration with detrimental effects. Artworks made with oil paints consist of several layers each with specific functions, such as adhesion to the substrate (ground layer), pictorial layers, color saturation and protection from the environment (varnish layer). Understanding the detailed composition of works of art is an tough analytical challenge since paint films consist of slowly evolving heterogeneities at the micro-<sup>1,2</sup> and nano-scales.<sup>3</sup> However, some chemical reactions such as the formation of metal soaps have been found

to occur frequently in oil paintings and have recently stimulated significant efforts to understand their initiation and progression.<sup>4</sup> The reactivity of lead white (hydrocerussite) and zinc white (zinc oxide) is well known.<sup>4</sup> Besides Pb and Zn, other elements, including Al, K, Ca, Cu, Cd, Mn form metal soaps in works of art.<sup>4,5</sup> Numerous factors (e.g., water, volatile acids, temperature, pigment dissolution, etc.) initiate and promote soap formation. Subsequently, complex and poorly understood processes yield, in some cases, disfiguring and disruptive metal soap aggregates. To mitigate such outcomes and understand which factors promote soap formation and aggregation, it is

necessary to investigate the distributions of chemical species in historical oil paints at multiple scales.

These studies typically require analysis of small paint cross sections to distinguish original species from alteration products and to identify regions of reactivity or diffusion. Scanning electron microscopy with energy dispersive X-ray analysis (SEM-EDX) in concert with Fourier transform infrared microspectroscopy ( $\mu$ -FTIR) have been especially valuable.<sup>1, 2, 4, 6</sup> However, the spatial resolution of  $\mu$ -FTIR is typically limited to several micrometers,<sup>7</sup> which is inadequate to detect species with low average concentrations and to resolve micro- and nano-scale heterogeneities within the paint or at the pigment-binder interfaces where reactions likely initiate. Novel photothermal IR spectroscopy methods<sup>8-10</sup> overcome these limitations by circumventing the diffraction limit of IR light. Optical photothermal infrared (O-PTIR) spectroscopy yields IR spectra and maps with  $\approx 500$  nm spatial resolution employing a visible-light laser beam to probe the photothermal expansion of the sample due to IR light absorption.<sup>9</sup> In the field of art conservation, O-PTIR has recently enabled the characterization of chemical complexes within the stratigraphy of very small paint cross sections.<sup>11</sup> Photothermal induced resonance (PTIR)<sup>8, 10</sup> yields IR spectra and maps with 10 nm to 20 nm spatial resolution<sup>12, 13</sup> by using an atomic force microscope (AFM) probe tip to transduce the photothermal expansion of a sample caused by light absorption.<sup>8, 10</sup> Recently, we leveraged PTIR, also known as AFM-IR, to identify and map the distributions of three chemically distinct and spatially intermingled metal soaps in a naturally aged oil paint sample.<sup>3</sup>

Here, an array of chemically sensitive methods (SEM-EDX, FTIR, O-PTIR, PTIR) is used to study the distribution of chemical phases at multiple length scales in the top layer of a French nineteenth-century painting *Gypsy Woman with Mandolin* (c. 1870) by Jean-Baptiste-Camille Corot (Figure 1a). Murky paint on much of the background (see Figure 1) was determined to be an anachronistic addition painted over original paint and ought to be removed to restore the painting's original appearance. Previous observations<sup>14</sup> indicated this layer contained lead white ( $2\text{PbCO}_3 \cdot \text{Pb}(\text{OH})_2$ ) and cobalt green ( $\text{Zn}_{1-x}\text{Co}_x\text{O}$ ,  $x < 0.3$ ) pigments along with metal soap alteration products. Studying the deterioration of this paint layer provides an opportunity to understand the pigment-oil chemistry better with the prospect of mitigating the occurrence of deleterious reactions.

For the thin cross-sections analyzed here ( $\approx 6$   $\mu\text{m}$  for  $\mu$ -FTIR,  $\approx 400$  nm for PTIR and O-PTIR) the scales probed by the IR experiments ( $\mu$ -FTIR  $\approx 2 \cdot 10^{11}$   $\text{nm}^3$ , O-PTIR  $\approx 10^8$   $\text{nm}^3$ , PTIR  $\approx 5 \cdot 10^3$   $\text{nm}^3$ ) reveal the presence and distribution of numerous distinct metal carboxylate species. The high signal-to-noise ratio, high spatial resolution ( $\approx 500$  nm), and moderate throughput of O-PTIR is ideal to identify species with low average concentration that are phase separated in small domains within paint films and species that have overlapping spectral features that are indistinguishable using techniques with lower spatial resolution. The spatial resolution of PTIR ( $\approx 10$  nm) is well suited to identify the distributions and associations of chemical species at the nanoscale. The O-PTIR and PTIR data presented here provide compelling evidence for the existence of many similar, though distinct, small ( $< 0.1$   $\mu\text{m}^3$ ) zinc carboxylate species and/or a range of chemical environments in which these complexes exist within the paint. This work shows that the

PTIR and O-PTIR provide access to new chemical information at the sub-micrometer and nanometer scales, which is required to advance our knowledge of the chemical processes occurring in oil paint.

## EXPERIMENTAL SECTION

### *Preparation of the cross section sample*

A small sample was excised from the painting using a surgical scalpel. It was embedded in a room-temperature curing styrene-polyester co-polymer block, which was ground to expose the paint stratigraphy and polished by hand using SiC grinding papers (240 to 600 grit) and polishing cloths (2400 to 8000 grit). Thin sections (either  $\approx 400$  nm or  $\approx 6$   $\mu\text{m}$  thick) were obtained from the polished cross-section sample using an ultramicrotome equipped with a diamond knife at  $45^\circ$ .

### *Synchrotron Fourier transform IR microspectroscopy ( $\mu$ -FTIR)*

The  $\approx 6$   $\mu\text{m}$  thick cross-section were placed between two KBr pellets and analyzed using a  $\mu$ -FTIR spectrometer coupled to the SMIS beam line at Synchrotron SOLEIL, France and a microscope equipped with a  $50 \times 50$   $\mu\text{m}^2$  narrow band MCT detector and a  $32\times$ , 0.65 numerical aperture (NA) objective. Spectra were collected in transmission mode from  $7500$   $\text{cm}^{-1}$  to  $750$   $\text{cm}^{-1}$ , accumulating 256 scans at each point with a spectral resolution of  $4$   $\text{cm}^{-1}$ . Both apertures were set to  $6.0$   $\mu\text{m}$ , and the lateral step size of the stage was  $3.5$   $\mu\text{m}$ . Integrated absorption intensity maps were obtained by integrating the area under a spectral band defined by two frequency points, after subtracting the local baseline defined by the same two points.

### *Optical photothermal infrared (O-PTIR) spectroscopy*

O-PTIR data from  $\approx 400$  nm thick cross sections deposited on a ZnSe substrate were obtained in reflection mode using a commercially available instrument. The setup consists of an optical microscope equipped with a reflective objective ( $40\times$ , 0.78 NA, 8 mm working distance), a pulsed quantum cascade laser (QCL), tunable from  $920$   $\text{cm}^{-1}$  to  $1800$   $\text{cm}^{-1}$  and  $2660$   $\text{cm}^{-1}$  and  $3020$   $\text{cm}^{-1}$ , a continuous wave visible detection laser ( $532$  nm, collinear with the QCL excitation laser), and a silicon photodetector. O-PTIR spectra were normalized with respect to the wavelength-dependent excitation laser intensity, which was measured using a broadly IR absorbing substrate (low emissivity glass) at a laser pulse rate of  $100$  kHz. All O-PTIR spectra ( $2$   $\text{cm}^{-1}$  spectral resolution, 10 averages) were obtained by pulsing the excitation laser at  $100$  kHz and sweeping the laser wavelength at a rate of  $100$   $\text{cm}^{-1}\text{s}^{-1}$ . O-PTIR maps were obtained by tuning the IR laser to a fixed frequency while the sample stage was scanned at  $1$  Hz. Images were collected using a stage step size of  $100$  nm.

### *Photothermal induced resonance (PTIR) spectroscopy*

For PTIR measurements, the  $\approx 400$  nm nominally thick samples were placed on a ZnSe substrate and measured using a modified commercially available instrument, consisting of an AFM microscope coupled to a QCL laser, tunable from  $1380$   $\text{cm}^{-1}$  to  $1900$   $\text{cm}^{-1}$ . Spectra and maps were obtained in tapping mode using a gold-coated cantilever ( $40$  N/m nominal spring constant) and by focusing the IR laser onto the sample at  $\approx 20^\circ$  angle from the substrate surface, using p-polarized light. The tapping-mode PTIR signal was demodulated using a heterodyne detection scheme employing a lock-in amplifier.<sup>3</sup> Briefly, the AFM cantilever was driven (tapped) at the second

mechanical bending mode frequency ( $f_2 \approx 1550$  kHz), the PTIR signal demodulated at the first bending frequency ( $f_1 \approx 250$  kHz) while the QCL was pulsed at  $f_{\text{Laser}} = f_2 - f_1 \approx 1300$  kHz. Maps were obtained by maintaining the wavelength constant while scanning the sample. Spectra were recorded with the AFM tip at a given location and sweeping the laser wavelength at  $50 \text{ cm}^{-1}\text{s}^{-1}$ . The spectra ( $2 \text{ cm}^{-1}$  resolution) were slightly smoothed using a Savitzky-Golay Filter (2<sup>nd</sup> order, 4 adjacent points) and normalized with respect to the laser intensity recorded using a power meter. The whole apparatus was purged with dry nitrogen. The pixel resolution of each image is specified in each figure caption. The spatial resolution of the PTIR maps is not estimated for every map since it depends on multiple parameters, including tip-sample interactions, sample stratification, and excitation frequency; however, the spatial resolution cannot be better than twice the pixel size.

## RESULTS AND DISCUSSION

Since preliminary investigation had revealed the presence of metal soaps,<sup>14</sup> paint samples were obtained to identify the pigments and the distribution of original paint components and alteration products. A cross-section sample (sample 1) and a paint scraping from the deteriorated green overpaint (sample 2) were obtained from the marked locations (X and O, respectively) at the top left-hand corner of the painting (Figure 2a). Visible and backscatter electron (BSE) images in Figure 2b, c show that the paint cross section consists of thirteen layers. A description of the sample stratigraphy is given in Figure S1 and Table S1 of the supporting information. Here, we focus only on the topmost layer containing the metal soaps (layer 13) to identify and map original materials and alteration products.

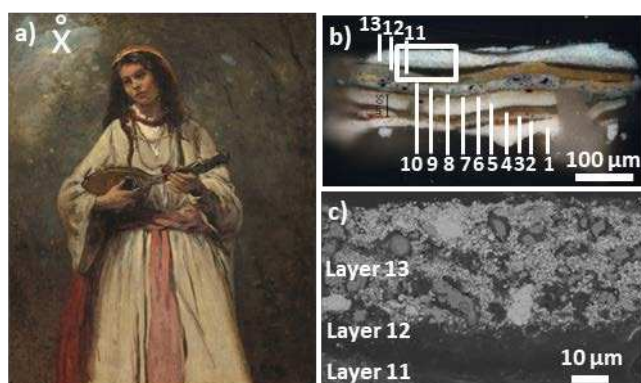


Figure 1. (a) Jean -Baptiste-Camille Corot, Gypsy Woman with Mandolin, c. 1870 (courtesy National Gallery of Art, Washington, D.C.). (b) OM image of cross section (sample 1) obtained using dark field reflected visible light illumination.; (c) BSE image of the area inside the white rectangle in (b).

A BSE image of layer 13 (Figure 2a) shows rounded particles ( $\approx 2 \mu\text{m}$  to  $\approx 5 \mu\text{m}$  diameter) intermingled with smaller ( $1 \mu\text{m}$  long) particles with higher atomic weight (brighter features). The morphology and EDX spectra from sample 1 thin section (Figure 2) show that the small, high-atomic-weight particles are lead white. The larger particles predominantly consist of Zn and O, with additional Co, Mg and Al. These are cobalt green, nominally  $\text{Zn}_{1-x}\text{Co}_x\text{O}$ , and match an historical pigment from the Forbes Pigment collection 9.05.05, “Cobalt Green Light” (see

Figure 2b). Hereafter, “Cobalt Green Light” is used to denote this historical pigment. Previous SEM-EDX analyses of this painting and “Cobalt Green Light” revealed cobalt blue ( $\text{CoAl}_2\text{O}_4$ ) impurities are the source of Al. Since the SEM-EDX maps of Mg and Zn for sample 2 (Figure S2) are for the most part overlapped, and Mg can form solid solutions with  $\text{ZnO}$ <sup>15</sup> and even  $\text{ZnCoO}$ <sup>16</sup>, it is likely that Mg is mostly present in low concentration within the cobalt green particles. However, a few Mg-rich particles are also detected (Figure S2c) and are tentatively assigned to a hydroxy magnesium carbonate phase (see SI). BSE images in Figure 1c and 2) show that many cobalt green particles are surrounded by a low atomic weight (dark in the BSE images, e.g., site III) phase. EDX analysis indicates this phase contains mainly C, O, Zn, and Mg (Figure 2c).

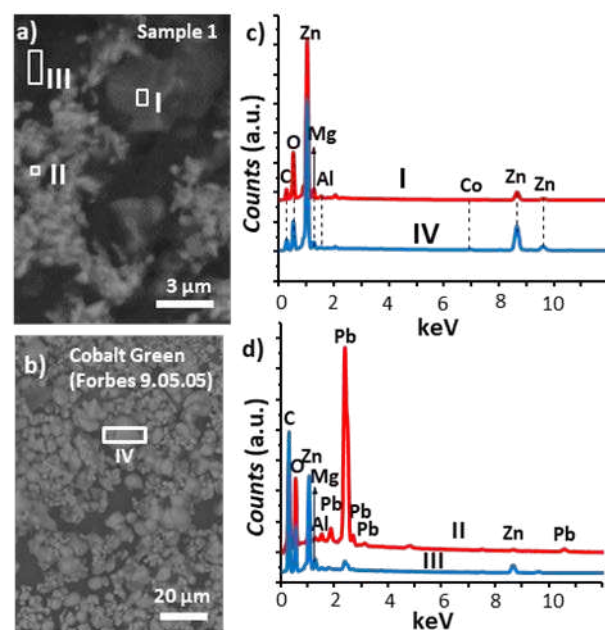


Figure 2. (a) BSE detail of layer 13 in sample 1; (b) BSE image of “Cobalt Green Light.” (c) EDX spectra of cobalt green particles in sample 1 from area I and from area IV in “Cobalt Green Light” pigment. (d) EDX spectra of areas II and III in panel a.

To determine the composition of this phase we employed 3 IR microscopy techniques. Representative  $\mu$ -FTIR spectra (Figure 3a) from a  $\approx 6 \mu\text{m}$  thick cross section containing a cobalt green particle were obtained at the marked positions (see inset), nominally, on the cobalt green particle (2), close to its boundary (1 and 3) and far from it (4). The spectra are all similar. Characteristic bands of oil:  $1743 \text{ cm}^{-1}$  ( $\nu_{\text{as}}(\text{C}=\text{O})$  ester),  $1467 \text{ cm}^{-1}$  ( $\delta(\text{CH}_2)$ ,  $\delta(\text{CH}_3)$ ),  $1413 \text{ cm}^{-1}$  ( $\omega(\text{CH}_2)$  in  $(\text{CH}_2-\text{COO})$  deformation),  $1378 \text{ cm}^{-1}$  ( $\omega(\text{CH}_2)$  in methyl chain) are observed in all four spectra. A shoulder at  $1711 \text{ cm}^{-1}$  on the ester carbonyl band indicates free carboxylic acids are present, meaning that not all carboxylic groups are converted to carboxylates. This observation is corroborated by the high-resolution O-PTIR and PTIR spectra (see below). While thermodynamics drive the reaction between free carboxylic groups and ionic species, the kinetics of this process can be affected by the local water content and site accessibility, which is likely impeded in some locations. A prominent broad band at  $\approx 1590 \text{ cm}^{-1}$  common to all spectra is attributed to  $\nu_{\text{as}}(\text{COO}^-)$  of the zinc carboxylate species

frequently seen in 19<sup>th</sup> and 20<sup>th</sup> century ZnO-containing paint.<sup>17-20</sup> In our previous work,<sup>3</sup> we referred to this peak as “zinc carboxylate” which was also observed in model paint films of cobalt green in linseed oil (1593 cm<sup>-1</sup>).<sup>5</sup> This peak was previously ascribed to a ionomeric phase<sup>17</sup> and later shown to comprise contributions from a few tetrahedral Zn-carboxylate species with relative IR intensities affected by the water content.<sup>21</sup> Here, we refer to this complex peak as disordered tetrahedral Zn-carboxylates (d-t-Zn-soap).

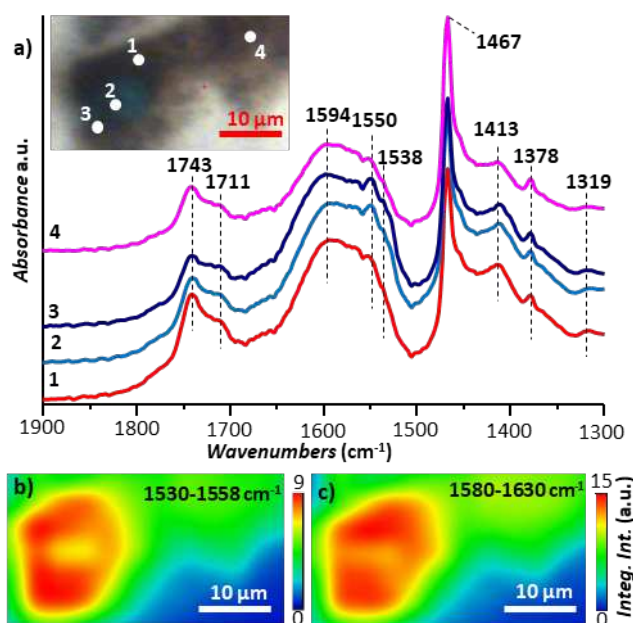


Figure 3. (a)  $\mu$ -FTIR spectra of a  $\approx 6 \mu\text{m}$  thick sample 1 cross section obtained at the marked locations (see inset). Corresponding  $\mu$ -FTIR intensity maps integrated between (b) 1530 cm<sup>-1</sup> to 1558 cm<sup>-1</sup> and (c) 1580 cm<sup>-1</sup> to 1630 cm<sup>-1</sup>.

The characteristic peaks of saturated or mono-unsaturated fatty acid zinc soaps are present but relatively weak, making the distinction between soaps such as zinc stearate/palmitate ( $\nu_{\text{as}}(\text{COO}^-) \approx 1540 \text{ cm}^{-1}$ ) or zinc oleate ( $\nu_{\text{as}}(\text{COO}^-) \approx 1549 \text{ cm}^{-1}$  and  $1527 \text{ cm}^{-1}$ ),<sup>22,23, 24</sup> and disordered lead soaps (broad band at  $\approx 1530 \text{ cm}^{-1}$ ) challenging. Since the narrow band of  $\nu_{\text{as}}(\text{COO}^-)$  of lead stearate at  $1513 \text{ cm}^{-1}$  is not observed and the BSE images do not suggest the presence of lead soaps, we conclude that soaps in this sample are primarily Zn soaps and not Pb soaps.

The integrated FTIR absorption intensity maps show similar (i.e., overlapping) distributions for crystalline zinc carboxylates ( $1530 \text{ cm}^{-1}$  to  $1558 \text{ cm}^{-1}$  Figure 3b) and d-t-Zn-soap ( $1580 \text{ cm}^{-1}$  to  $1630 \text{ cm}^{-1}$ , Figure 3c) phases, consistent with the small spectra variation. This is not surprising since the cobalt green particles ( $\approx 2 \mu\text{m}$  to  $\approx 5 \mu\text{m}$ ) are smaller than both the sample thickness ( $\approx 6 \mu\text{m}$ ) and  $\mu$ -FTIR resolution ( $\approx 6 \mu\text{m}$ ). Spectrum 2, for example, is an average of the cobalt green particle (that, if unaltered, does not have any IR absorption features above  $1200 \text{ cm}^{-1}$ ) and the surrounding areas containing both oil and the zinc soaps. Therefore, assessment of the distribution of metal soaps in these samples requires a higher IR spatial resolution.

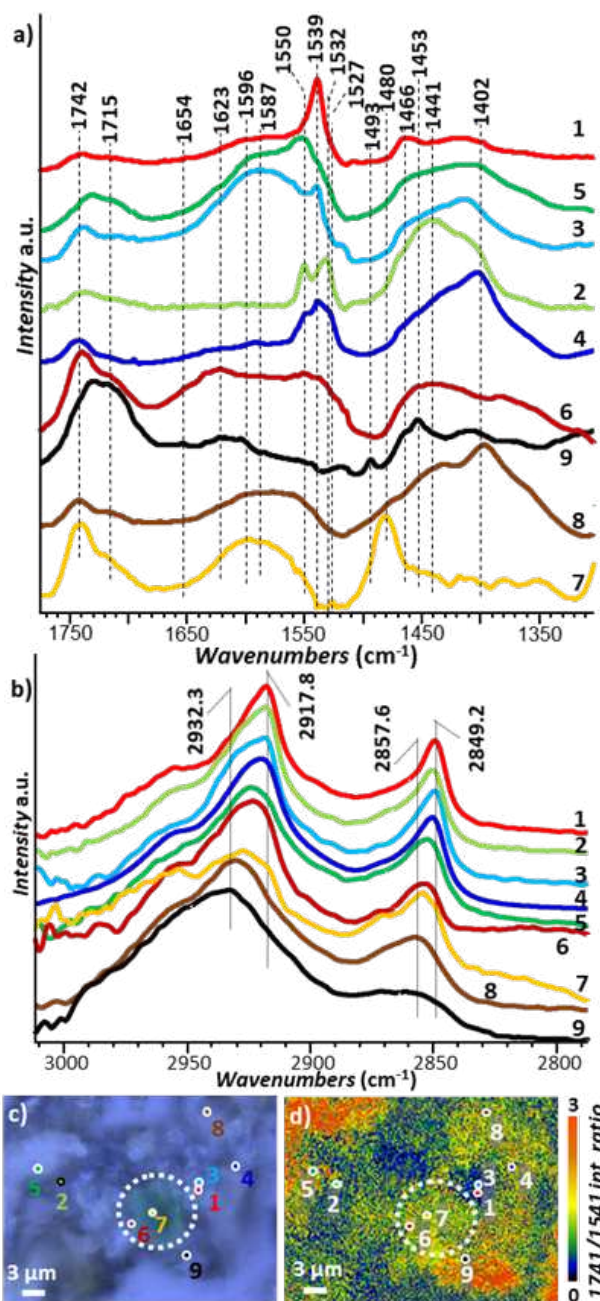


Figure 4. (a, b) O-PTIR spectra from a 400 nm thick section of layer 13 obtained at the color-coded locations in panel c and d in the proximity of a cobalt green particle roughly delineated by the dotted circles. (c) Optical microscopy image. (d) O-PTIR intensity ratio map obtained by pixel-wise division of the intensity at  $1741 \text{ cm}^{-1}$  (oil) by the intensity at  $1541 \text{ cm}^{-1}$  ( $\text{Zn}(\text{St})_2$ ).

O-PTIR is an emerging contactless technique that overcomes the diffraction-limited spatial resolution of traditional IR microscopy providing submicron ( $\approx 500 \text{ nm}$ ) resolution. O-PTIR uses a pulsed IR laser to induce a photothermal response of the sample (thermal expansion and thermally-induced change of the refractive index). This response is detected by monitoring the intensity of a diffraction-limited collinear visible laser. Although the O-PTIR spectra are recorded here in reflection, the

photothermal effect ensures that the O-PTIR spectra are intrinsically dependent on the imaginary part of the refractive index and therefore are directly comparable with spectra in traditional transmission FTIR databases. This characteristic aids spectral interpretation and material identification, thus addressing challenges unmet by conventional IR microscopy in many applications, such as life sciences,<sup>25, 26</sup> polymer composites,<sup>27</sup> and microplastics<sup>28</sup> In cultural heritage applications, O-PTIR was recently used to reveal the stratigraphy of very small paint cross sections.<sup>11</sup> In this study, we take advantage of a recently introduced QCL laser that covers the C–H stretching and the finger print spectral regions.

Figure 4a shows a selection of the most diverse and distinct O-PTIR spectra obtained from a  $\approx 400$  nm thick cross section in proximity of a cobalt green particle. Compared to  $\mu$ -FTIR (Figure 3), the O-PTIR spectra (Figure 4a) reveal an astonishingly heterogeneous chemical composition at the  $\approx 500$  nm scale. For the thin samples studied here, O-PTIR probes the composition of the entire sample thickness, thus the heterogeneity observed is not confined to interfacial boundaries or the paint-air interface. Since the volume of the sample probed by O-PTIR ( $\approx 0.5 \times 0.5 \times 0.4 \mu\text{m}^3$ ) is approximately 2000-fold smaller than the volume probed by  $\mu$ -FTIR ( $\approx 6 \times 6 \times 6 \mu\text{m}^3$ ), O-PTIR spectra reveals species that are locally ( $\approx 0.1 \mu\text{m}^3$  scale) more abundant than in the average composition at the scale probed by synchrotron  $\mu$ -FTIR ( $\approx 200 \mu\text{m}^3$ ). This is particularly useful to identify metal soaps that tend to phase separate at micro- and nanoscales<sup>3</sup> (see below) and typically have distinct but spectrally close IR absorption frequencies.<sup>23</sup> The O-PTIR spectra show both crystalline zinc carboxylate phases ( $1530$ - $1558 \text{ cm}^{-1}$ , sharp peaks) and disordered Zn-soap phases ( $1550$ - $1660 \text{ cm}^{-1}$ , broad peaks) coexisting within the  $0.1 \mu\text{m}^3$  volume probed. We observe the characteristic peaks of zinc stearate ( $1539 \text{ cm}^{-1}$ ,  $\text{ZnSt}_2$ ), zinc oleate ( $1550 \text{ cm}^{-1}$ ,  $1527 \text{ cm}^{-1}$ ,  $\text{ZnOl}_2$ ) and possibly zinc azelate ( $1550 \text{ cm}^{-1}$ ,  $1532 \text{ cm}^{-1}$ ,  $\text{ZnAz}_2$ ). The  $\text{ZnSt}_2$  peak at  $1539 \text{ cm}^{-1}$  is often dominant among the crystalline carboxylate phases (see Figure S3). The characteristic peak of magnesium stearate ( $\approx 1572 \text{ cm}^{-1}$ ,  $\text{MgSt}_2$ )<sup>29</sup> is absent. The broad peak centered around  $1590 \text{ cm}^{-1}$ , typically associated with Zn carboxylates<sup>3</sup> or an ionomeric phase,<sup>17</sup> shows large variations in central frequency, shape, and full width at half maximum (Figure 4a), suggesting it is associated with significant chemical heterogeneity. Spectra in Figure 4 show broad features in this range with slightly resolved peaks at  $1654 \text{ cm}^{-1}$ ,  $1623 \text{ cm}^{-1}$ ,  $1587 \text{ cm}^{-1}$ , and  $1554 \text{ cm}^{-1}$ . The spectral shifts and differences in peak shape are likely due to variations in the local coordination environment and/or water content and are attributed to a tetrahedral Zn soap phase<sup>21</sup> (see discussion below). Importantly, the classification of the crystalline Zn carboxylate phases, based on sharp peaks between  $1530 \text{ cm}^{-1}$  and  $1558 \text{ cm}^{-1}$ , and disordered tetrahedral Zn-soap phases, with broad peaks between  $1550 \text{ cm}^{-1}$  and  $1660 \text{ cm}^{-1}$  correlates well with the  $\text{CH}_2$  stretching frequencies (Figure 4b). It is well known that the frequencies of the  $\text{CH}_2$  symmetric and antisymmetric stretching of aliphatic chains strongly depend on the chains' intramolecular conformation.<sup>30, 31</sup> When the characteristic sharp peaks of crystalline Zn soaps are most prominent in the spectra, the  $\nu_{\text{as}}(\text{CH}_2)$  frequency is lowest ( $\approx 2918 \text{ cm}^{-1}$ ), but it increases substantially (up to  $\approx 2932 \text{ cm}^{-1}$ ) when only peaks from disordered Zn soaps are observed in the spectra (spectra 5, 7, 8, 9 in Figure 4b). When evidence for ordered and disordered metal soap phases

coexists in the spectra, both low and high frequency  $\nu_{\text{as}}(\text{CH}_2)$  contributions are observed (see light spectrum 3 in Figure 4b). Given the  $100 \text{ nm}$  step size,  $\approx 500 \text{ nm}$  lateral resolution,  $\approx 0.1 \mu\text{m}^3$  probed volume, the relative IR intensities of metal soap species in our sample change abruptly (see Figure S3) suggesting that phase separation in the sample occurs on length scales shorter than  $500 \text{ nm}$ . O-PTIR maps display some contrast between  $\text{ZnSt}_2$  rich areas (blue) and oil-rich areas (orange) at this scale but the resolution is insufficient to clearly identify of boundaries (see Figure 4d and Figure S3).

By transducing the photothermal expansion of the sample with an AFM probe tip, PTIR yields absorption spectra with  $10 \text{ nm}$  to  $20 \text{ nm}$  spatial resolution,<sup>8, 10</sup> which, critically, are not limited by heat diffusion.<sup>32-33</sup> Since PTIR is a photothermal method, its signal is proportional to the sample absorption coefficient<sup>34, 35</sup> (i.e., the imaginary part of the refractive index) thus enabling identification of materials<sup>3, 36</sup> by comparison with IR spectral databases. Generally, PTIR is not a surface-selective technique and has been shown to probe sample compositions at depths exceeding  $1 \mu\text{m}$ ,<sup>37</sup> and even underneath a  $\approx 200 \text{ nm}$  thick material when operating in contact mode.<sup>38</sup> Here, however, we use the recently introduced tapping-mode PTIR measurement paradigm<sup>3</sup> that probes the sample composition  $\approx 50 \text{ nm}$  deep<sup>39</sup> by exploiting the tip enhancement and the non-linear tip-sample mechanical interactions during the tapping cycle to generate the heterodyned signal. Therefore, we estimate that the sample volume probed in the tapping PTIR experiments is  $\approx 10 \times 10 \times 50 \text{ nm}^3$  (i.e.,  $\approx 5000 \text{ nm}^3$ ) which permits revealing compositional details much smaller than the sample thickness.

The PTIR spectra resemble the O-PTIR spectra in Figure 4. The characteristic peaks of oil:  $1741 \text{ cm}^{-1}$  ( $\nu_{\text{a}}(\text{C}=\text{O})$  ester),  $1464 \text{ cm}^{-1}$  ( $\delta(\text{CH}_2)$ ,  $\delta(\text{CH}_3)$ ),  $1413 \text{ cm}^{-1}$  ( $\omega(\text{CH}_2)$ ),  $1380 \text{ cm}^{-1}$  show a location-dependent relative intensities, better visualized in the PTIR map at  $1740 \text{ cm}^{-1}$  in Figure 5d; The shoulder at  $\approx 1710 \text{ cm}^{-1}$  on the ester carbonyl band suggests that free carboxylic acids are also present. The reconstructed image of ester carbonyl (red) and carboxylic acid (blue) absorptions (Figure 5e) show that, except for a very small area with no carboxylic groups, these two phases coexist at the nanoscale in slightly varying proportions (purple).

The PTIR spectra (Figure 5a, Figure S5a and Figure S6a) indicate the presence of crystalline ( $1530 \text{ cm}^{-1}$  to  $1558 \text{ cm}^{-1}$ ) and disordered tetrahedral Zn ( $1570 \text{ cm}^{-1}$  to  $1660 \text{ cm}^{-1}$ ) metal soaps in relative abundances that are location dependent. We attribute the peaks at  $1538 \text{ cm}^{-1}$  and at  $1549 \text{ cm}^{-1}$  to  $\text{Zn}(\text{St})_2$  and  $\text{Zn}(\text{Ol})_2$ , respectively, as for O-PTIR spectra (Figure 5a). The broad peak at  $\approx 1596 \text{ cm}^{-1}$  (Figure 5a) displays different peak shapes with shoulders at  $1615 \text{ cm}^{-1}$  and  $1623 \text{ cm}^{-1}$ . The distribution of  $\text{ZnSt}_2$  and d-t-Zn-soap are shown in Figure 5b and 5c respectively. The disordered tetrahedral Zn carboxylate phase is widespread, and its spatial distribution (green) together with  $\text{ZnSt}_2$  (red) and  $\text{ZnOl}_2$  (blue) is displayed in Figure 5f.  $\text{ZnSt}_2$  and  $\text{ZnOl}_2$  are associated closely but not overlapping (Figure 5f).

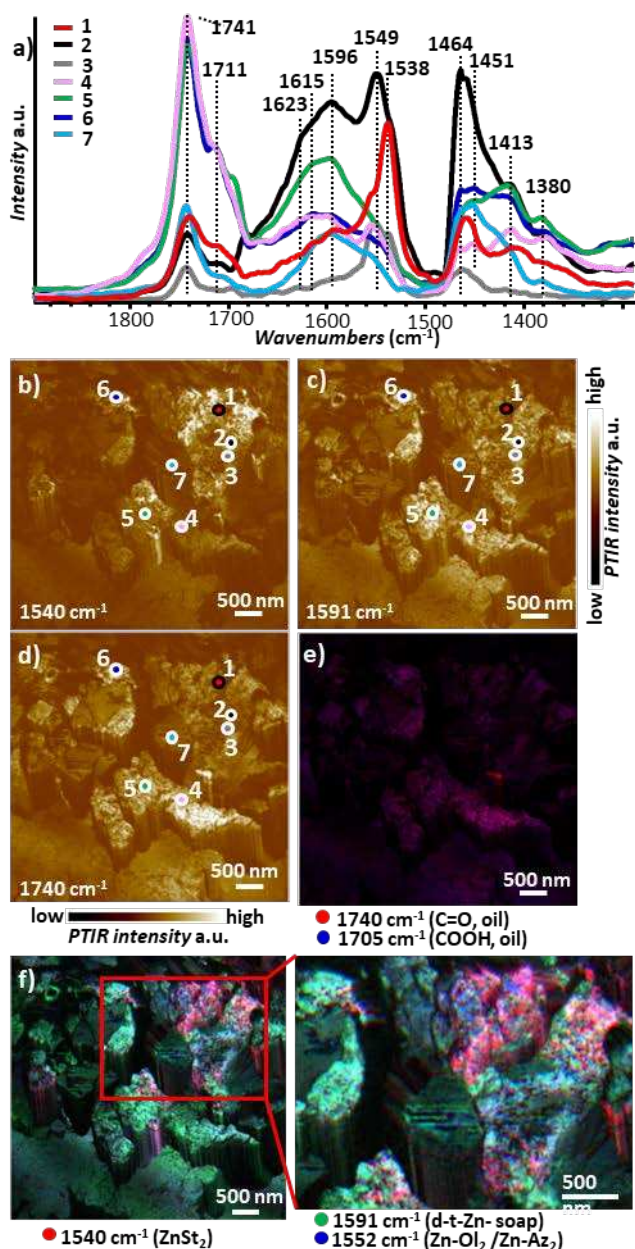


Figure 5. (a) PTIR spectra from a  $\approx 400$  nm thick cross section, obtained at the color-coded locations in panels b-d. PTIR absorption maps at: (b)  $1541\text{ cm}^{-1}$  ( $\text{ZnSt}_2$ ), (c)  $1591\text{ cm}^{-1}$  (tetrahedral Zn-carboxylate) and (d)  $1740\text{ cm}^{-1}$  (oil). (e) Reconstructed qualitative color-coded map of PTIR absorption at:  $1740\text{ cm}^{-1}$  (red, ester carbonyl) and  $1705\text{ cm}^{-1}$  (blue, carboxylic acid). (f) Reconstructed qualitative color-coded map of PTIR absorption displaying  $\text{ZnSt}_2$  ( $1540\text{ cm}^{-1}$ , red), tetrahedral Zn-carboxylate ( $1591\text{ cm}^{-1}$ , green), and  $\text{ZnOl}_2/\text{Zn-Az}_2$  ( $1552\text{ cm}^{-1}$ , blue). Inset: magnified view of the area delimited by the red rectangle in f. Colors in panels e, f, are not displayed on a common intensity scale. PTIR images were acquired with a pixel size of  $12.6\text{ nm}$  and  $49.2\text{ nm}$  in the horizontal and vertical directions, respectively.

The d-t-Zn-soap band ( $\approx 1596\text{ cm}^{-1}$ ), commonly observed in paint samples,<sup>4</sup> was previously attributed to a ionomeric

phase.<sup>17</sup> This broad peak presents location-dependent spectral maxima at  $1654\text{ cm}^{-1}$ ,  $1623\text{ cm}^{-1}$ ,  $1554\text{ cm}^{-1}$  (Figure 4a)  $1623\text{ cm}^{-1}$  and  $1615\text{ cm}^{-1}$  (Figure 5a)  $1643\text{ cm}^{-1}$ ,  $1615\text{ cm}^{-1}$ ,  $1600\text{ cm}^{-1}$  and  $1583\text{ cm}^{-1}$  (Figure S6a),  $1628\text{ cm}^{-1}$ ,  $1615\text{ cm}^{-1}$ ,  $1598\text{ cm}^{-1}$  and possibly  $1577\text{ cm}^{-1}$  (Figure S5a). Such a complex band raises the question whether it stems from the convolution of widely different chemical species that incidentally have overlapping or partially overlapping absorption peaks, or by just one or a few chemical moieties that are characterized by slightly different arrangements or local environment due to variations in density, water content, intermolecular interactions or other conditions. Metal oxalates,<sup>40</sup> for example, have peaks in the  $1610\text{ cm}^{-1}$  to  $1665\text{ cm}^{-1}$  spectral range. However, the diagnostic, but somewhat weaker, metal oxalate doublet (i.e.,  $1364\text{ cm}^{-1}$  and  $1320\text{ cm}^{-1}$  for zinc oxalate) is not observed in either PTIR or O-PTIR spectra, making the assignment to metal oxalates unlikely. Some mixed-metal carboxylate phases, such as  $\text{ZnNa}_2\text{St}_4$  and  $\text{ZnK}_2\text{St}_4$  have peaks in this region ( $1608\text{ cm}^{-1}$  to  $1620\text{ cm}^{-1}$ ).<sup>41, 42</sup> Figure 2 shows that Mg and Zn are present in the region surrounding the cobalt green particles. Conceivably, a mixed Mg-Zn carboxylate phase with peaks in this region could exist, but we are unable to confirm it. No evidence of a characteristic peak at  $1577\text{ cm}^{-1}$  for  $\text{MgSt}_2$ <sup>29</sup> was obtained. Figure S2 shows that Mg is a minor constituent of the cobalt green particles but we cannot confirm it from the IR spectra since  $\text{Zn}_{1-x}\text{Mg}_x\text{O}$ ,  $x < 0.49$ <sup>15</sup> peaks at  $\approx 1400\text{ cm}^{-1}$  and  $\approx 1600\text{ cm}^{-1}$ ,<sup>43</sup> and the associated water absorption at  $\approx 1630\text{ cm}^{-1}$  overlap with Zn-carboxylate and oil peaks. The few Mg-rich particles identified in Figure S2 are tentatively attributed to hydromagnesite,  $\text{Mg}_5(\text{CO}_3)_4(\text{OH})_2 \cdot 4\text{H}_2\text{O}$  that has a strong absorption at  $\approx 1480\text{ cm}^{-1}$  (see spectrum 7 in Figure 4).

Attenuated total reflection (ATR) FTIR spectra on a model paint have convincingly shown that the broad  $\approx 1590\text{ cm}^{-1}$  peak can be attributed to the superposition of at least three distinct, broad peaks ( $1625\text{ cm}^{-1}$ ,  $1595\text{ cm}^{-1}$  and  $1555\text{ cm}^{-1}$ ) due to tetrahedrally coordinated Zn carboxylates<sup>21</sup> that are better resolved in dry samples. Peaks at  $1625\text{ cm}^{-1}$  and at  $1555\text{ cm}^{-1}$  were attributed to tetrahedral Zn chain-like complexes and a peak at  $1595\text{ cm}^{-1}$  to a tetrahedral Zn oxo-complex cluster within an ionomeric phase. A tetrahedral Zn oxo cluster is commonly observed in Zn-based metal-organic frameworks (MOFs) that, however, are not stable in humid environments.<sup>44, 45</sup> For example, the asymmetric carboxylate stretch of prototypical Zn-based MOF-5 shifts from  $\approx 1602\text{ cm}^{-1}$  to  $\approx 1595\text{ cm}^{-1}$  in ATR-FTIR spectra<sup>44</sup> when exposed to moisture due to partial hydrolysis of the Zn-oxide clusters.<sup>45</sup> Therefore, it is not surprising that the characteristics of the peak at  $\approx 1595\text{ cm}^{-1}$  depend strongly on the water content in the paint.<sup>21</sup> While the degradation of crystalline Zn MOFs is typically irreversible, the spectral characteristics of the model paint were recovered upon hydration.<sup>21</sup> Since, with respect to a dry sample, the relative intensity of the  $1595\text{ cm}^{-1}$  peak was shown to increase under normal humid conditions but the Zn oxo cluster of MOFs is unstable in humid conditions,<sup>44, 45</sup> spectral changes in this region are more likely linked to similar and probably heterogeneous assemblies of tetrahedral Zn carboxylate species with relative proportions that are a function of the water content within the disordered or ionomeric phase.<sup>21</sup> Ionomers are polymers with neutral and ionized pendant chemical moieties (typically carboxylic acids/carboxylates) covalently bonded to the polymer backbone. In ionomers,  $< 15\%$  of the pendant groups are ionized leading to  $\approx 1$

nm to 5 nm<sup>46-49</sup> ionic-rich hydrophilic domains that upon water absorption can become interconnected via small (< 1 nm) secondary domains. Ionomers typically have small (< 5 nm) randomly distributed (semi)crystalline domains often lacking long-range order embedded within an amorphous ionomeric matrix.<sup>46-49</sup> Therefore, ionomer domains ( $\approx 5 \text{ nm}^3$  to  $500 \text{ nm}^3$ ) are much smaller than the volume probed by O-PTIR ( $\approx 10^8 \text{ nm}^3$ ), yet O-PTIR spectra show significant heterogeneity for this Zn soap band in our sample (Figure 4a). The sample volume ( $\approx 5000 \text{ nm}^3$ ) probed by PTIR is also too large to resolve the chemical heterogeneities of a typical ionomeric phase if present. Careful observation of the distribution of  $1591 \text{ cm}^{-1}$  and  $1610 \text{ cm}^{-1}$  absorption features (Figure S4g and S5b, i.e., within the broad d-t-Zn-soap peak) reveals only partial overlap and some heterogeneous regions with dimensions up to  $\approx 100 \text{ nm}$  (Figure S4g) and up to  $\approx 500 \text{ nm}$  (Figure S5b), much larger than the heterogeneities typical of ionomers (1 nm to 5 nm).<sup>46</sup> The observation of tetrahedrally coordinated Zn carboxylates peaks that emerge as a function of the water content in model paint<sup>50</sup> make it tempting to attribute the heterogeneities in Figure S4g and S5b to tetrahedrally coordinated Zn carboxylates that are partially hydrolyzed to different extents.

The PTIR map at  $1408 \text{ cm}^{-1}$  (Figure S4a, f, h) shows lead white particles that appear ellipsoidal in the two-dimensional PTIR absorption maps (see SI for details). Although not the focus of this work, the ability to map inorganic phases with a lower thermal expansion coefficient than the surrounding, embedding phase could be beneficial for studying complex mixtures such as paint. Analysis of a smoother cross section at even higher spatial resolution (Figure S6) shows an example where  $\text{ZnSt}_2$  ( $1539 \text{ cm}^{-1}$ , Figure S6c) and d-t-Zn-soap ( $1613 \text{ cm}^{-1}$ , Figure S6d) phases are closely intermingled, but clearly separated at the nanoscale (see the reconstructed image overlay in Figure S6e). Figure S7 shows a map with < 4 nm spatial resolution, possibly the highest ever reported for PTIR,<sup>10</sup> and reveals features smaller than 15 nm.

## CONCLUSIONS

In this work, high resolution, chemically sensitive methods (SEM-EDX,  $\mu$ -FTIR, O-PTIR, PTIR) are used to study the distribution of chemical species and metal soaps in the top paint layer of a French 19th century painting. O-PTIR and PTIR probe volumes that are  $\approx 2000 \times$  and  $\approx 10^7 \times$  smaller than the volumes probed by synchrotron  $\mu$ -FTIR, yielding compositional information at the scales required to advance our knowledge of the chemical processes occurring in paints. Improvements in sample preparation protocols to yield thinner and smoother cross-sections will further facilitate PTIR and O-PTIR investigations on paint and other complex mixtures.

Assuming the same spectral acquisition time for each of the three techniques,  $\mu$ -FTIR chemical imaging throughput is at least 3 and 6 to 7 orders of magnitude higher than O-PTIR and PTIR, respectively, due to the much bigger pixel sizes. Therefore, these methods are most advantageous when used in concert. PTIR provides the highest spatial resolution and enables assessing the fine distribution of separated phases in paint, although at slow pace. O-PTIR enables the rapid identification of species that are locally more abundant than in the average paint composition and strikes an excellent balance between spatial

resolution, throughput, and information content. The lower resolution and higher throughput of  $\mu$ -FTIR enables measurement of entire paint sections and is most useful for assessing chemical gradients and dynamic changes in paint.<sup>1, 3, 51</sup>

The paint samples analyzed here are mixtures comprising pigments, cured oil, crystalline metal soaps with characteristic narrow IR peaks ( $\approx 1530 \text{ cm}^{-1}$  to  $1558 \text{ cm}^{-1}$ ) and a heterogeneous, disordered, water-permeable partially hydrolyzed, metal soap phase with characteristic broad IR peaks ( $\approx 1570 \text{ cm}^{-1}$  to  $1660 \text{ cm}^{-1}$ ) which was previously assigned to an ionomeric phase. The PTIR and O-PTIR data reported here appear incompatible with a strict interpretation of the typical ionomer structure (i.e., polymers, with less than 15 % of ionized pendant chemical moieties that form very small,  $\approx 5 \text{ nm}^3$  to  $500 \text{ nm}^3$ , heterogeneous domains). However, we believe that some ionomer-like properties at a longer scale (e.g., matrix with ionized pendant groups with water-dependent percolation pathways and morphology) are useful to describe this complex phase. This can be rationalized by the fact that the polymerized paint network is not copolymerized by a few monomeric species but likely by a greater variety of species that result in a range of locally ionized group densities and domain sizes. This interpretation is further supported by the observation of free carboxylic acid groups ( $\approx 1710 \text{ cm}^{-1}$ ) through the paint network across all the scales probe here.

Here, we show that the polymeric paint network associated with a broad and complex peak at  $\approx 1596 \text{ cm}^{-1}$  has a high degree of conformational disorder (gauche defects), indicated by the  $\nu_{\text{as}}(\text{CH}_2)$  stretching frequencies (Figure 4). Spectra obtained with nanoscale spatial resolution reveal several overlapping spectral features contributing to the broad band that we assign principally to partially hydrolyzed tetrahedral Zn carboxylates that have different structural arrangements and/or water content. High-resolution IR maps show that the crystalline metal soap phases ( $\text{ZnSt}_2$ ,  $\text{ZnOl}_2$ ) in our samples are closely intermingled with the disordered tetrahedral Zn-soap phases but clearly separated from them, in agreement with previous observations.<sup>3</sup>

This work highlights the potential of using IR spectroscopy techniques operating at different length scales to probe the evolution of alteration products in chemically complex systems, which is necessary to understand the chemistry of paints. We believe that this work will stimulate robust work to determine the nanoscale composition of oil paints and foster the development of art preservation and conservation practices.

## ASSOCIATED CONTENT

### Supporting Information

Additional experimental details, sample description, BSE, EDX, O-PTIR and PTIR data are available in the supporting information free of charge on the ACS Publications website.

## AUTHOR INFORMATION

### Corresponding Author

\* Barbara Berrie. Scientific Research Department, National Gallery of Art, 2000B South Club Drive, Landover, Maryland, 20785, USA. E-mail: [B-BERRIE@NGA.GOV](mailto:B-BERRIE@NGA.GOV)

\* Andrea Centrone. Nanoscale Device Characterization Division, Physical Measurement Laboratory, National Institute of Standards

and Technology, 100 Bureau Drive, Gaithersburg, MD, 20899, USA. E-mail: [andrea.centrone@nist.gov](mailto:andrea.centrone@nist.gov)

## Author Contributions

The manuscript was written through contributions of all authors. All authors have approved the final version of the manuscript.

## Notes

The authors declare no competing financial interest.

## ACKNOWLEDGMENT

Xiao Ma was the Charles E. Culpeper Advanced Fellow in Conservation Science in the scientific research department at the National Gallery of Art during 2017-2019. J.J.S. acknowledges support under the Corporative Research Agreement Award 70NANB14H209, through the University of Maryland. Kathryn Harada, graduate intern (2016-2017), painting conservation department of National Gallery of Art, sampled the painting and assisted with the pigment analysis. She and Melanie Gifford are thanked for insightful discussions.

## REFERENCES

- Gabrieli, F.; Rosi, F.; Vichi, A.; Cartechini, L.; Pensabene Buemi, L.; Kazarian, S. G.; Miliani, C., *Anal. Chem.* **2017**, *89* (2), 1283-1289.
- Keune, K.; Boon, J. J., *Stud. Conserv.* **2007**, *52* (3), 161-176.
- Ma, X.; Beltran, V.; Ramer, G.; Pavlidis, G.; Parkinson, D. Y.; Thoury, M.; Meldrum, T.; Centrone, A.; Berrie, B. H., *Angew. Chem. Int. Ed.* **2019**, *58* (34), 11652-11656.
- Casadio, F.; Keune, K.; Noble, P.; Loon, A. V.; Hendriks, E.; Centeno, S. A.; Osmond, G., *Metal Soaps in Art: Conservation and Research*. Springer: 2019.
- Mazzeo, R.; Prati, S.; Quaranta, M.; Joseph, E.; Kendix, E.; Galeotti, M., *A Anal. Bioanal. Chem.* **2008**, *392* (1), 65-76.
- Van der Weerd, J.; Brammer, H.; Boon, J. J.; Heeren, R. M. A., *Appl. Spectrosc.* **2002**, *56* (3), 275-283.
- Petibois, C.; Piccinini, M.; Guidi, M. C.; Marcelli, A., *J. Synchrotron Radiat.* **2010**, *17* (1), 1-11.
- Centrone, A., *Annu. Rev. Anal. Chem.* **2015**, *8* (1), 101-126.
- Zhang, D.; Li, C.; Zhang, C.; Slipchenko, M. N.; Eakins, G.; Cheng, J.-X., *Sci. Adv.* **2016**, *2* (9), e1600521.
- Kurouski, D.; Dazzi, A.; Zenobi, R.; Centrone, A., *Chem. Soc. Rev.* **2020**, *49* (11), 3315-3347.
- Beltran, V.; Marchetti, A.; Nuyts, G.; Leeuwestein, M.; Sandt, C.; Borondics, F.; De Wael, K., *Angew. Chem. Int. Ed.* **2021**, *60* (42), 22753-22760.
- Katzenmeyer, A. M.; Holland, G.; Kjoller, K.; Centrone, A., *Anal. Chem.* **2015**, *87* (6), 3154-3159.
- Wieland, K.; Ramer, G.; Weiss, V. U.; Allmaier, G.; Lendl, B.; Centrone, A., *Nano Res.* **2019**, *12* (1), 197-203.
- Ma, X.; Hageraats, S.; Beltran, V.; Thoury, M.; Refregiers, M.; Keune, K.; Berrie, B. H., *Microsc. Microanal.* **2018**, *24* (S1), 2152-2153.
- Park, W. I.; Yi, G.-C.; Jang, H. M., *Appl. Phys. Lett.* **2001**, *79* (13), 2022-2024.
- Singh, V. P.; Singh, R. K.; Das, D.; Rath, C., *Mater. Sci. Semicond. Process.* **2013**, *16* (3), 659-666.
- Hermans, J. J.; Keune, K.; van Loon, A.; Iedema, P. D., *J. Anal. At. Spectrom.* **2015**, *30* (7), 1600-1608.
- Osmond, G., Zinc White and the Influence of Paint Composition for Stability in Oil Based Media. In *Issues in Contemporary Oil Paint*, van den Berg, K. J.; Burnstock, A.; de Keijzer, M.; Krueger, J.; Learner, T.; de Tagle, A.; Heydenreich, G., Eds. Springer International Publishing: Cham, 2014; pp 263-281.
- Osmond, G.; Boon, J. J.; Puskar, L.; Drennan, J., *Appl. Spectrosc.* **2012**, *66* (10), 1136-1144.
- Helwig, K.; Monaghan, M.; Poulin, J.; Henderson, E. J.; Moriarty, M.; Rita, *Stud. Conserv.* **2020**, 1-15.
- Hermans, J. J.; Baij, L.; Koenis, M.; Keune, K.; Iedema, P. D.; Woutersen, S., *Sci. Adv.* **2019**, *5* (6), eaaw3592.
- Helwig, K.; Poulin, J.; Corbeil, M.-C.; Moffatt, E.; Duguay, D., Conservation Issues in Several Twentieth-Century Canadian Oil Paintings: The Role of Zinc Carboxylate Reaction Products. In *Issues in Contemporary Oil Paint*, van den Berg, K. J.; Burnstock, A.; de Keijzer, M.; Krueger, J.; Learner, T.; Tagle, d. A.; Heydenreich, G., Eds. Springer International Publishing: Cham, 2014; pp 167-184.
- Otero, V.; Sanches, D.; Montagner, C.; Vilarigues, M.; Carlyle, L.; Lopes, J. A.; Melo, M. J., *J. Raman Spectrosc.* **2014**, *45* (11-12), 1197-1206.
- Robinet, L.; Corbeil, M.-C., The Characterization of Metal Soaps. *Stud. Conserv.* **2003**, *48* (1), 23-40.
- Spadea, A.; Denbigh, J.; Lawrence, M. J.; Kansiz, M.; Gardner, P., *Anal. Chem.* **2021**, *93* (8), 3938-3950.
- Wang, A. J.; Dillon, E. P.; Maharjan, S.; Liao, K.-S.; McElhenny, B. P.; Tong, T.; Chen, S.; Bao, J.; Curran, S. A., Resolving, *Adv. Mater. Interfaces.* **2021**, *8* (5), 2001720.
- Olson, N. E.; Xiao, Y.; Lei, Z.; Ault, A. P., *Anal. Chem.* **2020**, *92* (14), 9932-9939.
- Kansiz, M.; Dowling, L. M.; Yousef, I.; Guaitella, O.; Borondics, F.; Sulé-Suso, J., *Anal. Chem.* **2021**, *93* (32), 11081-11088.
- Herm, C. In *Infrared Spectroscopic Study of some more Metal Soaps*, The Sixth Infrared and Raman Users Group Conference, IRUG, 2004; pp 267-272.
- Centrone, A.; Hu, Y.; Jackson, A. M.; Zerbi, G.; Stellacci, F., *Small* **2007**, *3* (5), 814-817.
- Snyder, R. G.; Scherer, J. R.; Gaber, B. P., *Biochim. Biophys. Acta - Biomembr.* **1980**, *601*, 47-53.
- Katzenmeyer, A. M.; Holland, G.; Chae, J.; Band, A.; Kjoller, K.; Centrone, A., *Nanoscale* **2015**, *7* (42), 17637-17641.
- Morozovska, A. N.; Eliseev, E. A.; Borodinov, N.; Ovchinnikova, O. S.; Morozovsky, N. V.; Kalinin, S. V., *Appl. Phys. Lett.* **2018**, *112* (3), 033105.
- Dazzi, A.; Glotin, F.; Carminati, R., *J. Appl. Phys.* **2010**, *107* (12), 124519.
- Ramer, G.; Akshuk, V. A.; Centrone, A., *Anal. Chem.* **2017**, *89* (24), 13524-13531.
- Schwartz, J. J.; Chuang, H.-J.; Rosenberger, M. R.; Sivaram, S. V.; McCreary, K. M.; Jonker, B. T.; Centrone, A., *ACS Appl. Mater. Interfaces* **2019**, *11* (28), 25578-25585.
- Lahiri, B.; Holland, G.; Centrone, A., *Small* **2013**, *9* (3), 439-445.
- Schwartz, J. J.; Le, S. T.; Krylyuk, S.; Richter, C. A.; Davydov, A. V.; Centrone, A., *Nanophotonics* **2021**, *10* (5), 1517-1527.
- Mathurin, J.; Deniset-Besseau, A.; Bazin, D.; Dartois, E.; Wagner, M.; Dazzi, A., *J. Appl. Phys.* **2022**, *131* (1), 010901.
- Monico, L.; Rosi, F.; Miliani, C.; Daveri, A.; Brunetti, B. G., *Acta A Mol. Biomol. Spectrosc.* **2013**, *116*, 270-280.
- Lah, N.; Rep, G.; Šegedin, P.; Golič, L.; Leban, I., *AACTA Crystallogr. C Struct. Chem.* **2000**, *56* (6), 642-643.
- Hermans, J. J.; Keune, K.; van Loon, A.; Corkery, R. W.; Iedema, P. D., *T Polyhedron* **2014**, *81*, 335-340.
- Hoggas, K.; Nouveau, C.; Djelloul, A.; Bououdina, M., *Appl. Phys. A* **2015**, *120* (2), 745-755.
- Rodríguez, N. A.; Parra, R.; Grella, M. A., *RSC Adv* **2015**, *5* (89), 73112-73118.
- Ming, Y.; Kumar, N.; Siegel, D. J., *ACS Omega* **2017**, *2* (8), 4921-4928.
- Kusoglu, A.; Weber, A. Z., *Chem. Rev.* **2017**, *117* (3), 987-1104.
- Allen, F. I.; Comolli, L. R.; Kusoglu, A.; Modestino, M. A.; Minor, A. M.; Weber, A. Z., *ACS Macro Lett.* **2015**, *4* (1), 1-5.
- Kusoglu, A.; Dursch, T. J.; Weber, A. Z., *Adv. Funct. Mater.* **2016**, *26* (27), 4961-4975.
- McLean, R. S.; Doyle, M.; Sauer, B. B., *Macromolecules* **2000**, *33* (17), 6541-6550.
- Baij, L.; Hermans, J. J.; Keune, K.; Iedema, P., *Angew. Chem. Int. Ed.* **2018**, *57* (25), 7351-7354.
- Possenti, E.; Colombo, C.; Realini, M.; Song, C. L.; Kazarian, S. G., *Anal. Bioanal. Chem.* **2021**, *413* (2), 455-467.

## TOC Figure

---

